



ARL-TR-7441 • SEPT 2015



US Army Research Laboratory

# **Spectroscopic Properties of Neodymium and Erbium-Doped Magnesium Oxide Ceramics**

**by T Sanamyan, C Cooper, G Gilde, A C Sutorik, and  
M Dubinskii**

Approved for public release; distribution unlimited.

## **NOTICES**

### **Disclaimers**

The findings in this report are not to be construed as an official Department of the Army position unless so designated by other authorized documents.

Citation of manufacturer's or trade names does not constitute an official endorsement or approval of the use thereof.

Destroy this report when it is no longer needed. Do not return it to the originator.



# **Spectroscopic Properties of Neodymium and Erbium-Doped Magnesium Oxide Ceramics**

**by T Sanamyan and M Dubinskii**

*Sensors and Electron Devices Directorate, ARL*

**C Cooper and G Gilde**

*Weapons and Materials Research Directorate, ARL*

**A C Sutorik**

*Dow Corning, Midland, MI*

REPORT DOCUMENTATION PAGE				Form Approved OMB No. 0704-0188	
<p>Public reporting burden for this collection of information is estimated to average 1 hour per response, including the time for reviewing instructions, searching existing data sources, gathering and maintaining the data needed, and completing and reviewing the collection information. Send comments regarding this burden estimate or any other aspect of this collection of information, including suggestions for reducing the burden, to Department of Defense, Washington Headquarters Services, Directorate for Information Operations and Reports (0704-0188), 1215 Jefferson Davis Highway, Suite 1204, Arlington, VA 22202-4302. Respondents should be aware that notwithstanding any other provision of law, no person shall be subject to any penalty for failing to comply with a collection of information if it does not display a currently valid OMB control number.</p> <p><b>PLEASE DO NOT RETURN YOUR FORM TO THE ABOVE ADDRESS.</b></p>					
1. REPORT DATE (DD-MM-YYYY) Sep 2015		2. REPORT TYPE Final		3. DATES COVERED (From - To)	
4. TITLE AND SUBTITLE Spectroscopic Properties of Neodymium and Erbium-Doped Magnesium Oxide Ceramics				5a. CONTRACT NUMBER	
				5b. GRANT NUMBER	
				5c. PROGRAM ELEMENT NUMBER	
6. AUTHOR(S) T Sanamyan, C Cooper, G Gilde, A C Sutorik, and M Dubinskii				5d. PROJECT NUMBER	
				5e. TASK NUMBER	
				5f. WORK UNIT NUMBER	
7. PERFORMING ORGANIZATION NAME(S) AND ADDRESS(ES) US Army Research Laboratory ATTN: RDRL-SEE-L 2800 Powder Mill Road Adelphi, MD 20783-1138				8. PERFORMING ORGANIZATION REPORT NUMBER  ARL-TR-7441	
9. SPONSORING/MONITORING AGENCY NAME(S) AND ADDRESS(ES)				10. SPONSOR/MONITOR'S ACRONYM(S)	
				11. SPONSOR/MONITOR'S REPORT NUMBER(S)	
12. DISTRIBUTION/AVAILABILITY STATEMENT Approved for public release; distribution unlimited.					
13. SUPPLEMENTARY NOTES					
14. ABSTRACT We present the results of development and comprehensive characterization of fully densified erbium (Er <sup>3+</sup> ): magnesium oxide (MgO) and neodymium (Nd <sup>3+</sup> ):MgO transparent ceramics fabricated from specially formulated nanopowders. The results are presented with major emphasis on potential laser application and the outlook for substantially improved laser power scaling at room temperature based on unique thermal properties of the host material. Also presented are the spectroscopic characterization results (absorption, fluorescence, and emission lifetimes) of Er <sup>3+</sup> and Nd <sup>3+</sup> dopant ions in the temperature range from 10 to 300 K. To the best of our knowledge, this is the first reported successful demonstration of MgO host material doping with rare earth (RE) ions. Spectroscopic results are indicative of single-site RE ion incorporation with nearly perfect single-crystalline environment within the MgO ceramic grains. Obtained experimental data can be used for assessing these materials as potential gain media for high power laser applications.					
15. SUBJECT TERMS ceramic, Al <sub>2</sub> O <sub>3</sub> , MgO, alumina, spectroscopy, laser					
16. SECURITY CLASSIFICATION OF:			17. LIMITATION OF ABSTRACT  UU	18. NUMBER OF PAGES  28	19a. NAME OF RESPONSIBLE PERSON Tigran Sanamyan
a. REPORT Unclassified	b. ABSTRACT Unclassified	c. THIS PAGE Unclassified			19b. TELEPHONE NUMBER (Include area code) 301-394-2044

## Contents

---

<b>List of Figures</b>	<b>iv</b>
<b>Acknowledgments</b>	<b>v</b>
<b>1. Introduction</b>	<b>1</b>
<b>2. Material Synthesis, Preparation and Characterization During the Processing</b>	<b>2</b>
<b>3. Results of the Material Synthesis</b>	<b>5</b>
<b>4. Spectroscopic Characterization</b>	<b>9</b>
4.1 Nd <sup>3+</sup> :MgO	10
4.2 Er <sup>3+</sup> :MgO	10
4.3 Emission	11
4.4 Absorption	13
<b>5. Conclusions</b>	<b>14</b>
<b>6. References</b>	<b>16</b>
<b>List of Symbols, Abbreviations, and Acronyms</b>	<b>18</b>
<b>Distribution List</b>	<b>20</b>

## List of Figures

Fig. 1	XRD patterns of Er,Li:MgO ceramic after treatment at different temperatures. MgO peaks are unlabeled and peaks due to $\text{Er}_2\text{O}_3$ are labeled “E”.....	6
Fig. 2	XRD patterns of Er,Li:MgO ceramic after treatment at different temperatures with the scale expanded to highlight the weak peaks due to $\text{Er}_2\text{O}_3$ (labeled “E”).....	7
Fig. 3	XRD patterns of Nd,Li:MgO ceramic after treatment at different temperatures with the scale expanded to highlight the weak peaks due to $\text{Nd}_2\text{O}_3$ (labeled “N”).....	7
Fig. 4	a) Transparent pellet of $\text{Er}^{3+}$ :MgO ceramic; b) transmission spectrum of a 2-mm-thick $\text{Er}^{3+}$ :MgO ceramic (red curve) versus theoretical transmission limited by Fresnel reflections of the 2 polished sample interfaces (shown in blue).....	8
Fig. 5	SEM of Er,Li: MgO ceramic highlighting amorphous, carbon-rich impurities found in the intergranular region .....	9
Fig. 6	a) RT fluorescence spectrum of $\text{Nd}^{3+}$ -doped MgO ceramic (black) covering the spectral range of ${}^4\text{F}_{3/2} \rightarrow {}^4\text{I}_{13/2}$ , ${}^4\text{F}_{3/2} \rightarrow {}^4\text{I}_{11/2}$ and ${}^4\text{F}_{3/2} \rightarrow {}^4\text{I}_{9/2}$ inter-multiplet transitions. The fluorescence spectrum of $\text{Nd}^{3+}$ -doped YAG for the same range of transitions is shown (in red) for comparison. b) Fluorescence decay from the ${}^4\text{F}_{3/2}$ manifold of $\text{Nd}^{3+}$ in MgO. ....	10
Fig. 7	${}^4\text{I}_{13/2} \rightarrow {}^4\text{I}_{15/2}$ fluorescence kinetics of fully densified $\text{Er}^{3+}$ -doped MgO ceramic at room temperature .....	11
Fig. 8	Fluorescence spectra of $\text{Er}^{3+}$ doped MgO fully densified ceramic corresponding to the ${}^4\text{I}_{13/2} \rightarrow {}^4\text{I}_{15/2}$ transition in the temperature range of 10–300 K. ....	12
Fig. 9	Emission cross section of the ${}^4\text{I}_{13/2} \rightarrow {}^4\text{I}_{15/2}$ transition at RT (300 K, black) and cryogenic temperature (80 K, red, and 10 K, blue) in $\text{Er}^{3+}$ -doped MgO ceramic derived from Fuchtbauer-Ladenburg relation (Eq. 2) .....	13
Fig. 10	Absorption spectra of $\text{Er}^{3+}$ -doped MgO ceramic corresponding to the ${}^4\text{I}_{15/2} \rightarrow {}^4\text{I}_{13/2}$ inter-multiplet transitions in the temperature range of 10–300 K. Color-coding of the plots by temperature is presented on the inset. ....	13
Fig. 11	Absorption spectra of $\text{Er}^{3+}$ doped MgO ceramic corresponding to the ${}^4\text{I}_{15/2} \rightarrow {}^4\text{I}_{11/2}$ inter-multiplet transitions in the temperature range of 10–300 K. Color-coding of the plots by temperature is presented on the inset. ....	14

## Acknowledgments

---

We gratefully acknowledge financial support of this work by the High Energy Laser Joint Technology Office.

INTENTIONALLY LEFT BLANK.



## 1. Introduction

---

Thermal conductivity of the host is one of the most important thermal parameters determining suitability of a given laser material for high power laser applications. Indeed, low thermal conductivity of the laser material itself is an obvious bottleneck in the removal of heat deposited inside the gain medium (as an indivisible part of the pumping process) to a highly thermally conductive heat sink. Use of laser materials with thermal conductivity drastically exceeding the room temperature (RT) thermal conductivity (TC) of yttrium aluminum garnet (YAG), currently the most prevalent solid-state laser host, will result in significant power scaling of existing solid-state lasers without major design complications. TC of conventional laser materials, such as YAG and even fluorides (such as yttrium lithium fluoride [LiYF<sub>4</sub>]), is known to drastically improve (to about an order of magnitude) upon cryogenic cooling.<sup>1</sup> It is for this specific reason laser development based on cryogenic cooling of conventional laser media, YAG<sup>2</sup> and LiYF<sub>4</sub>,<sup>3</sup> has resulted in well-demonstrated ease of power scaling with nearly diffraction limited beam quality in very simple laser designs. We believe that similar results can be demonstrated at RT if laser materials with a RT TC significantly exceeding that of YAG become available.

A few recent efforts toward development of low-loss highly thermally conductive transparent ceramics<sup>4,5</sup> have shown some progress in this direction, but in both cases the target hosts were uniaxial. Thus, desirable transparency can only be achieved through further solid-state crystal conversion (SSCC)<sup>4</sup> or magnetic ceramic grain alignment,<sup>6</sup> which substantially complicates material development. In order to simplify the development, it is, perhaps, prudent to simply look for more promising high TC hosts among cubic materials. One of the most promising cubic host materials happens to be magnesium oxide (MgO). Indeed, single-crystalline MgO has a RT TC between ~60 and ~80 W/m·K,<sup>8</sup> which is gigantic compared to the RT TC of YAG (~10 W/m·K<sup>1</sup>) and should result in a desirable advance in laser power scalability. It is worth noting that single-crystalline MgO, doped by transition metal (TM) ions, such as chromium (Cr<sup>3+</sup>) and nickel (Ni<sup>2+</sup>), has already been reported as a laser host in the past. While the Cr<sup>3+</sup>:MgO laser has only been demonstrated with low optical-to-optical efficiency (2.3%) and low output power (under 50 mW),<sup>9</sup> the Ni<sup>2+</sup>:MgO laser has delivered output power as high as 9 W continuous wave (CW),<sup>10</sup> which was a clear manifestation of significant power-scaling potential. No further laser successes have been reported with transition metal doped single-crystalline MgO, perhaps due to significant difficulties with crystal growth of refractory MgO (melting point over 2852 °C per the Alfa Aesar

vendor). This is why the ceramic approach to obtaining optically clear MgO has a unique potential and is worth exploring.

Doping single-crystalline MgO host with rare-earth (RE) ions instead of TM ions can be extremely beneficial for laser power scaling. This is based on existing commercially available diode laser pump sources, as well as, in general, much longer upper laser level lifetimes of usable RE ions versus TM ions. Unfortunately, growing RE-doped MgO single crystals has proven to be elusive. Indeed, due to the significant ionic radius mismatch between the RE ions and the magnesium (Mg) ion of the host, RE elements exhibit negligible solubility within the MgO crystal structure and tend to not incorporate into the growing crystal. In the meantime, it has been demonstrated that bulk ceramics possess the capability to accommodate “less friendly” dopants and/or significantly higher dopant levels than melt-grown crystals while maintaining optical quality sufficient for laser applications.<sup>11</sup> This indicates that ceramic synthesis and processing allow for more “non equilibrium” dopant incorporation than traditional melt-growth techniques. Therefore, we believe, a ceramic approach must be adopted to bulk RE:MgO fabrication in order to achieve RE ion concentration sufficient for laser applications with laser-acceptable optical quality.

This report details the development and comprehensive characterization of fully densified erbium ( $\text{Er}^{3+}$ ):MgO and neodymium ( $\text{Nd}^{3+}$ ):MgO transparent ceramics from specially formulated nanopowders. We have achieved successful incorporation of sufficient amounts of  $\text{Er}^{3+}$  and  $\text{Nd}^{3+}$  into fully densified, transparent MgO ceramics. We also report the results of detailed spectroscopic investigation of  $\text{Er}^{3+}$ - and  $\text{Nd}^{3+}$ -doped MgO ceramics per this first attempt toward transparent bulk RE-doped MgO via ceramic synthesis and processing.

## **2. Material Synthesis, Preparation and Characterization During the Processing**

---

Er and Nd were chosen for doping for their well-known efficient performance as laser cations. The following materials were used for synthesis as received from their indicated vendor: MgO nanopowder, 15-nm average particle size, Nanocerox, Ann Arbor, MI; erbium(III) nitrate pentahydrate ( $\text{Er}(\text{NO}_3)_3 \cdot x\text{H}_2\text{O}$ ), 99.9%, Alfa Aesar, Ward Hill, MA; neodymium(III) nitrate hexahydrate ( $\text{Nd}(\text{NO}_3)_3 \cdot 6\text{H}_2\text{O}$ ), 99.9%, Alfa Aesar, Ward Hill, MA; lithium carbonate ( $\text{Li}_2\text{CO}_3$ ), 99.0% ACS grade, Alfa Aesar, Ward Hill, MA; poly(ethylene glycol) (PEG) 4000, FCC Grade Union Carbide, Danbury, CT; Triton X100, Union Carbide, Danbury, CT; oleic acid, technical grade, 90%, SigmaAldrich, St. Louis, MO; acetonitrile, HPLC grade, SigmaAldrich, St. Louis, MO.

The amounts of MgO, RE nitrate, and  $\text{Li}_2\text{CO}_3$  were mixed to give the intended stoichiometries of either  $\text{Er}_{0.00125}\text{Li}_{0.00125}\text{Mg}_{0.9975}\text{O}$  or  $\text{Nd}_{0.0005}\text{Li}_{0.0005}\text{Mg}_{0.999}\text{O}$ . Batch sizes were typically for 50 g of oxide product. Additionally, the following combination of commercial dispersants and binders were added to enhance processing and sintering of the starting MgO nanopowder: 5.4 wt % PEG 4000, 2.7 wt % Triton X100, and 2.7 wt % oleic acid. The starting materials were combined in 310 g acetonitrile; the solvent effectively disperses the MgO nanopowder into a slurry while dissolving all other components, allowing for their uniform distribution throughout the nanopowder. The mixture was stirred for approximately 1 h to homogenize, after which the slurry was transferred to a rotary evaporator. Acetonitrile was evaporated from the solids at 60 rpm, under reduced pressure. After the bulk of the solvent was removed, the remaining powder cake was transferred to a clean, loosely covered dish and placed in an oven at  $\sim 75^\circ\text{C}$  overnight to ensure complete evaporation. Finally, the powder was passed through a 60-mesh stainless steel sieve.

For sintering, the starting powders were first compacted into disk-shaped green bodies under 11 MPa uniaxial compression in 31.75-mm-diameter stainless steel dies. These were then vacuum-sealed in clean plastic bags and further compressed in a cold isostatic pressure vessel under 200 MPa. Pellets were sintered in an open air furnace with the following heating schedule: heat to  $800^\circ\text{C}$  at  $0.25^\circ\text{C}/\text{min}$  and hold for 4 h; cool to  $200^\circ\text{C}$  at  $3^\circ\text{C}/\text{min}$ ; heat to  $800^\circ\text{C}$  at  $1^\circ\text{C}/\text{min}$  and hold for 1 h; heat to  $1550^\circ\text{C}$  at  $1^\circ\text{C}/\text{min}$  and hold for 5 h; cool to RT at  $5^\circ\text{C}/\text{min}$ . The extended time and second cycle at  $800^\circ\text{C}$  were intended to allow for more complete burn out of the organic binders without introducing sudden thermal or physical stresses to the ceramic parts. Doped MgO samples at this point exhibited a faint translucency, closed porosity, and  $\sim 98\text{--}99\%$  of full density. Lastly, samples were heated in a hot isostatic pressure (HIP) furnace at  $1850$  or  $1950^\circ\text{C}$  (ramp rates of  $5^\circ\text{C}/\text{min}$ ) for 5 h under 200 MPa of argon, and final densities are universally  $>99\%$  of theoretical.

Powder x-ray diffraction (XRD) analysis was employed to determine the crystalline phases in doped MgO ceramics after the different sintering steps. Powders of sintered pellets were prepared by grinding fragments in a glass mortar and pestle to avoid crystalline contamination. Measurements were taken using a computer controlled Rigaku Miniflex operating at 30 kV and 15 mA with a step size of  $0.03^\circ 2\theta$  and scan rate of  $5^\circ 2\theta/\text{min}$ , scanning over  $5\text{--}60^\circ$ . Powder samples were loaded directly into low-background amorphous silicon (Si) sample holders.

A Hitachi 4700 scanning electron microscope (SEM) was used to observe the morphology of sintered ceramic grain structure. An accelerating voltage of 2 kV and beam current of  $\sim 10$  mA were used throughout this procedure in order to

minimize charging. The dopant concentration was measured by inductively coupled plasma-atomic emission spectroscopy (ICP-AES) method at Galbraith Laboratories.

The Archimedes method was used to determine the bulk density of the sintered pellets. Each pellet was first weighed to obtain the dry mass. They were then placed under vacuum in a closed vessel for 1 h. The vessel was backfilled with de-ionized water, and samples were left submerged for a few minutes to allow absorption of water into any available open porosity. The pellets were removed and wiped with a damp cloth to remove residual surface water. The wet pellets were then weighed immediately (before significant water evaporation could occur) in air (wet mass) and in a water submerged basket (submerged mass) using a Mettler Toledo AX205 balance. Using these values, the bulk density ( $\rho_{\text{Bulk}}$ ) was calculated as

$$\rho_{\text{bulk}} = \left( \frac{m_{\text{dry}}}{m_{\text{wet}} - m_{\text{submerged}}} \right) \rho_{\text{H}_2\text{O}} \quad (1)$$

where  $m$  is the mass of the dry, wet, and submerged pellet (as noted by a subscript), and  $\rho_{\text{H}_2\text{O}}$  is the density of water.

The ACTON 2500i spectrometer was used to obtain fluorescence spectra in the spectral range of 500–1200 nm, and Nicolet 6700 Fourier spectrometer was used to obtain fluorescence spectra in the wavelength range beyond 1200 nm. Both spectrometers were equipped with a standard commercial cryogenic dewar (Cryo Industries of America, Inc) allowing temperature control and measurements in the range of 10–300 K. The spectral resolution of the measurement setup was better than 1 nm at RT and 0.2 nm at cryogenic temperatures. The  $\text{Er}^{3+}$  energy levels around 10000–12000  $\text{cm}^{-1}$  were typically excited by diode lasers emitting at  $\sim 800$  and  $\sim 980$  nm. Occasionally, a tunable pulsed titanium (Ti)-sapphire laser was used for fluorescence excitation at shorter wavelengths. The spectral correction of the fluorescence spectra taken with both spectrometers has been performed using a standard calibrated quartz-halogen tungsten lamp (Optronic Laboratories, LLC). The  $\text{Er}^{3+}:\text{MgO}$  lifetime measurements in the temperature range of 10–300 K were conducted by using the  $\sim 10$ -ns pulses from tunable Ti:sapphire laser for excitation. A high-speed indium gallium arsenide (InGaAs) or Si detector attached to the ACTON 2500i monochromator was used for fluorescence decay measurements. In this case, the detector signal was processed using a TDS 2014 digital oscilloscope. The fluorescence spectrum in most instances was detected by a cooled InGaAs detector combined with a Stanford Research System SR 850 digital lock-in amplifier. The equipment control and data acquisition were integrated into a simple

LabVIEW based program. For signal acquisition, equipment control and processing the NI DAQmx USB 6210 device was used in LABVIEW environment.

### 3. Results of the Material Synthesis

---

To have potential as a laser gain medium, a candidate ceramic must demonstrate 2 crucial features: high transparency at the desired wavelengths of absorption and emission, and the ability to accommodate laser dopants in well-defined sites in its crystal structure. In addition to the favorable thermal properties discussed earlier, MgO has a long history of being prepared as fully dense ceramic with a transmission window from 250–8000 nm.<sup>12,13</sup> With multiple methods available for preparing pure MgO as transparent ceramic, the greatest issue with regard to engineering a laser host is the question of RE cation stability in the MgO crystal structure. The trivalent (3+) cations suffer from both size and charge mismatch, which makes direct substitution for  $\text{Mg}^{2+}$  more difficult and less likely under highly thermodynamic processes such as single crystal growth.

Low-temperature chemical synthesis methods, such as rapid co-precipitation of the mixed oxide from solution, have been shown to lead to RE incorporation into the MgO host.<sup>14</sup> Unfortunately, such powder precursor synthesis does not guarantee that the RE will remain in the lattice under the high temperatures needed to sinter the powder to a fully dense ceramic. Once diffusion is sufficiently thermally activated, the dopant cations may be able to migrate from the lattice and form their own separate oxides or a glassy intergranular phase. Not only would this render the system much less attractive for laser applications, but also the separate RE-containing species would represent scattering centers due to their different refractive index from the bulk MgO host, and transmission through the ceramic body would greatly reduce as a result.

Indeed, in our early experiments, where a ceramic synthesis was attempted using RE and MgO alone, it became apparent that such phase separation occurred readily during all steps of sintering. Even the high temperatures of the HIP step were insufficient to diffuse rare earth into the MgO lattice, or if they were, the exsolution of RE was too rapid to be quenched from high temperature. As such, trials with a co-dopant ion, which could aid in stabilizing RE in MgO, were attempted. Lithium (Li) was chosen because its cation size is much closer to that of  $\text{Mg}^{2+}$ ; it can diffuse readily into a variety of oxide lattices; and it offers a charge compensation scheme, which may be more conducive to doping in which 1  $\text{Li}^+$  and 1  $\text{RE}^{3+}$  substitute for every 2  $\text{Mg}^{2+}$  cations.

After the first sintering at an isotherm of 1550 °C for 5 h, the ceramics demonstrated high density, which varied only modestly with the RE cation used. For Er,Li:MgO

initial densities were 3.550–3.576 g/mL; for the Nd-containing ceramics, the values ranged from 3.547–3.555 g/mL. The theoretical density of MgO is 3.585 g/mL. After HIP treatment at either 1850 or 1950 °C, the average densities increase to  $3.623 \pm 0.010$  g/mL for Er,Li:MgO and  $3.607 \pm 0.010$  g/mL for Nd,Li:MgO. Using the target formulae for each composition as stated in the experimental and assuming no change to the MgO unit cell volume, the theoretical densities should increase only modestly to 3.599 g/mL (Er-doped) and 3.590 g/mL (Nd-doped). Although slightly higher than this simple model, there is at least a measure of consistency in the density trend, and it is indirectly supported by the fact that the translucency of the samples consistently increases after high temperature HIP, implying a reduction in scattering from residual porosity. Unfortunately, an alternate model is also possible. The densities of the respective oxides are themselves quite high (7.33 g/mL for neodymium oxide [Nd<sub>2</sub>O<sub>3</sub>] and 8.66 g/mL for erbium oxide [Er<sub>2</sub>O<sub>3</sub>]), and so these phases, if present, would contribute to densities that are higher than anticipated for the doped MgO.

Somewhat more conclusive information on the extent of successful RE doping was derived from the XRD analysis. Figure 1 shows the diffraction patterns of Er,Li:MgO ceramic after sintering at 1550 °C in air and 1850 or 1950 °C under HIP. At the displayed scale, the patterns are dominated by MgO with the peaks at 37.0, 42.9, 62.3, and 74.7° 2 $\theta$ , all accounted for by the known diffraction pattern (PDF # 45-946).

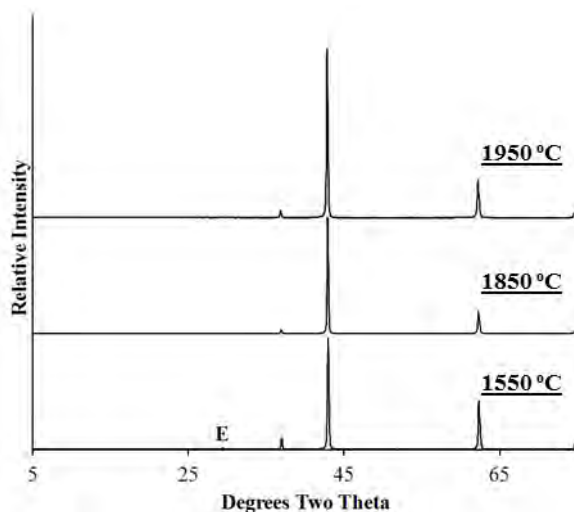


**Fig. 1** XRD patterns of Er,Li:MgO ceramic after treatment at different temperatures. MgO peaks are unlabeled and peaks due to Er<sub>2</sub>O<sub>3</sub> are labeled “E”.

However, a very weak peak appears just above the background at 29.4° 2 $\theta$ , the location of the 100% intensity peak of Er<sub>2</sub>O<sub>3</sub> (PDF # 8-50). (PDF # 8-50). Figure 2 shows an expanded scale view of the diffraction pattern highlighting 25–60° 2 $\theta$ . Not only is the peak at 29.4° 2 $\theta$  clearly observed, but several other weak peaks

associated with  $\text{Er}_2\text{O}_3$  can be detected. The fact that these peaks can be observed despite the low doping level suggests that the oxide detected is highly crystalline and diffracts strongly.

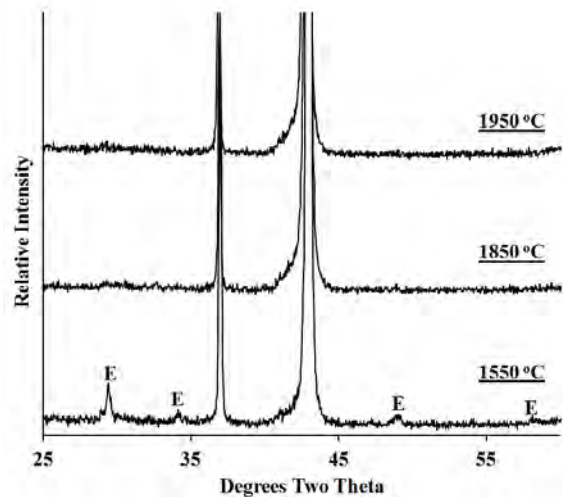


**Fig. 2** XRD patterns of Er,Li:MgO ceramic after treatment at different temperatures with the scale expanded to highlight the weak peaks due to  $\text{Er}_2\text{O}_3$  (labeled “E”)

These peaks are totally absent from the patterns of ceramics HIPed at both 1850 and 1950 °C. This means that within the detection limits of the XRD analysis,  $\text{Er}_2\text{O}_3$  which was present at the end of the air sintering step has diffused into the MgO lattice and is no longer present as a separate phase. Figure 3 shows the analogous series of XRD patterns for the Nd,Li:MgO samples, and similarly, weak  $\text{Nd}_2\text{O}_3$  peaks that are present in the 1550 °C sintered ceramic are gone after HIP at higher temperatures.

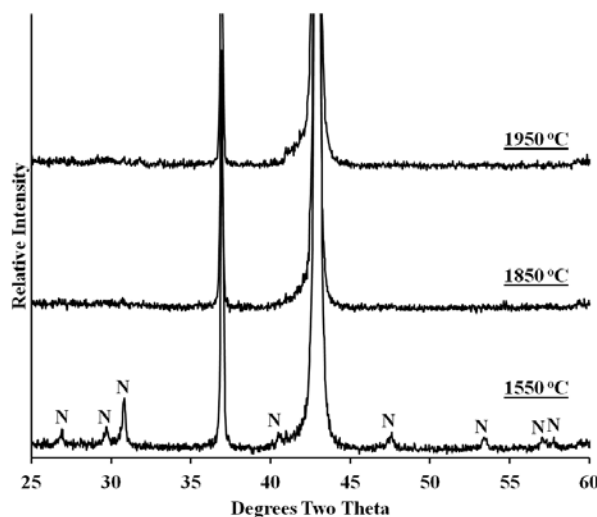


**Fig. 3** XRD patterns of Nd,Li:MgO ceramic after treatment at different temperatures with the scale expanded to highlight the weak peaks due to  $\text{Nd}_2\text{O}_3$  (labeled “N”)

By these observations, a significant level of RE doping into MgO has occurred. The possibility of volatilization of some of the RE can be somewhat discounted by 3 facts. Firstly, ICP-AES analysis of the Er content of Er,Li:MgO ceramic confirmed that the RE is present at a level close to the target composition (measured: 0.156 at % on the  $\text{Mg}^{2+}$  sited; theoretical: 0.125 at %). Although some experimental variations may contribute to the difference between the measured and expected values (such as varied hydration levels in the starting materials), there has clearly not been a loss of Er on high temperature processing. Secondly, in early trials, before  $\text{Li}^+$  was used as a co-dopant, the RE oxide persisted in the diffraction patterns of both systems after HIP treatment. Incorporation of  $\text{Li}^+$  apparently has a direct impact in aiding the diffusion of RE into the MgO at high temperatures as well as resulting in a visually noticeable improvement to ceramic transparency. Lastly, the spectroscopic behavior (absorption and fluorescence) of the ceramics, discussed below, corroborates that the RE cations have, in fact, found their way into highly crystalline sites in the host oxide.

Despite the similar XRD results, the Er- and Nd-doped samples demonstrate different degrees of transparency after HIP. The Nd-doped samples, although improving after HIP, display only weak translucency at best. The light transmission through Er, Li:MgO is significantly better. A photo of Er, Li: MgO resting on a page of type is shown in Fig. 4a, and a typical transmission spectrum is given in Fig. 4b. Although scattering is still clearly present, the Er-doped ceramics have achieved a promising level of translucency. The significant light scattering caused by residual pores<sup>15</sup> and phase impurities<sup>16</sup> in ceramics is well known, and their impact is so pronounced that the transmission will be affected by populations, which are too small to detect with other bulk methods. Hence, even when an XRD pattern is free of second phases, an amount below the instrument detection limit could still be a significant source of scatter.

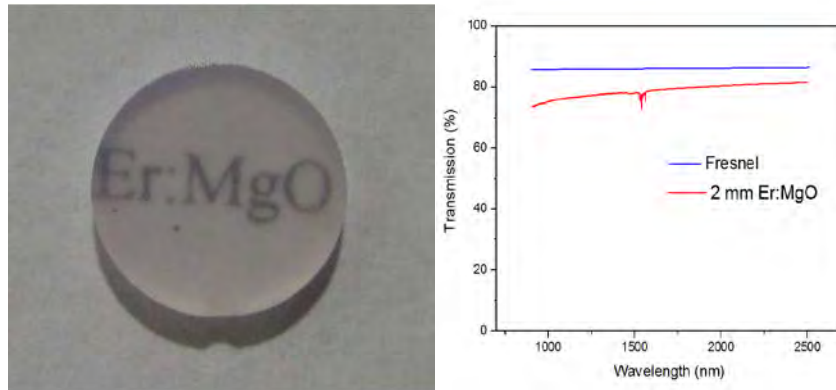


**Fig. 4** a) Transparent pellet of  $\text{Er}^{3+}:\text{MgO}$  ceramic; b) transmission spectrum of a 2-mm-thick  $\text{Er}^{3+}:\text{MgO}$  ceramic (red curve) versus theoretical transmission limited by Fresnel reflections of the 2 polished sample interfaces (shown in blue)



Since it appears to be the more promising of the current candidates in regard to forming a low scatter ceramic, the microstructure of Er,Li:MgO has been under investigation with SEM for clues as to the nature of the persistent scatter. A significant occurrence of either pores or RE oxide precipitates has not been found. Rather Fig. 5 illustrates one of some commonly observed amorphous features found in the intergranular region of the ceramic. Elemental analysis with energy dispersive spectroscopy shows that such features are usually rich in carbon, and so we strongly believe that such impurities forms from the thermal decomposition of the organic binders and dispersants used in the processing. We believe the issue of graphitic impurities can be eliminated, and experiments to address this issue through formulation modification and improved efficiency of the low temperature burn out are required.

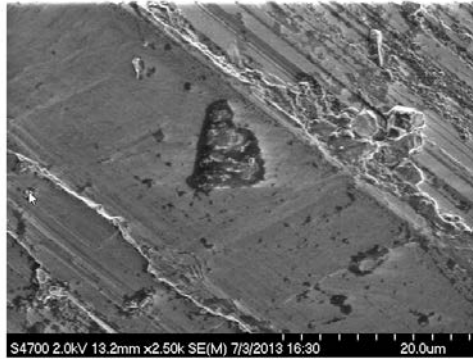


**Fig. 5 SEM of Er,Li: MgO ceramic highlighting amorphous, carbon-rich impurities found in the intergranular region**

#### **4. Spectroscopic Characterization**

The samples under investigation were Nd<sup>3+</sup>:MgO and Er<sup>3+</sup>:MgO ceramics prepared as described above. This represents procedures at their current best level of material optimization. All fully densified ceramic samples obtained under optimized fabrication conditions exhibited sharp, well-resolved absorption and emission lines characteristic of RE<sup>3+</sup> ions, thus also indicating well-defined, ordered, single-site RE<sup>3+</sup> occupation within single-crystalline MgO grains (see below).

The emissions associated with the  $^4I_{11/2} \rightarrow ^4I_{13/2}$  and  $^4I_{13/2} \rightarrow ^4I_{15/2}$  transitions of Er<sup>3+</sup> and  $^4F \rightarrow ^4I_{11/2}$  of Nd<sup>3+</sup> ions in MgO are of major practical interest since efficient, high power lasers based on these transitions have been successfully demonstrated in a variety of oxide laser hosts, even with much lower thermal conductivity than that of MgO. These lasers successfully operate with relatively low dopant concentrations and demonstrate high efficiencies at both room and cryogenic temperatures.<sup>17,18</sup>

## 4.1 Nd<sup>3+</sup>:MgO

The developed samples of Nd<sup>3+</sup>:MgO were still too high in scatter for absorption measurements, so their characterization at this point was limited to fluorescence measurements. The RT fluorescence spectrum of Nd<sup>3+</sup>-doped MgO ceramic in the spectral range spanning  $^4F_{3/2} \rightarrow ^4I_{13/2}$ ,  $^4F_{3/2} \rightarrow ^4I_{11/2}$  and  $^4F_{3/2} \rightarrow ^4I_{9/2}$  transitions, excited at 808 nm by a diode laser, is presented in Fig. 6a (black plot). For comparison, the Nd<sup>3+</sup>:YAG fluorescence spectrum (red plot) for the same spectral range is shown along with the Nd<sup>3+</sup>:MgO fluorescence. As Fig. 6a indicates, all of the fluorescence transitions from the  $^4F_{3/2}$  state of Nd<sup>3+</sup> in MgO exhibit narrow-line inter-Stark emissions grouping around 930–970, 1060–1080, and 1330–1350 nm, which crudely resemble those of Nd<sup>3+</sup> in YAG. The observed fluorescence decay from the  $^4F_{3/2}$  manifold of Nd<sup>3+</sup> in MgO, shown in Fig. 6b, was found to be nearly single exponential. The fluorescence lifetime measures in the range of 0.5–1 ms, and indicates some dependence on the sample preparation conditions.

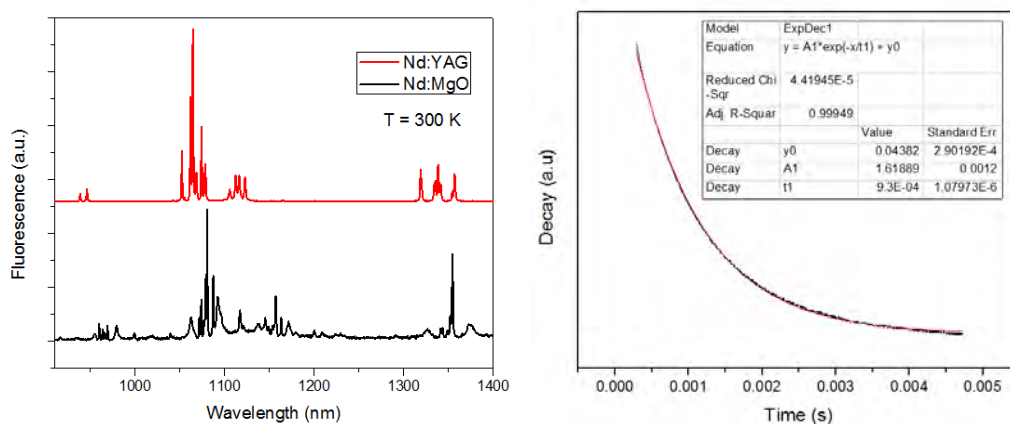


**Fig. 6** a) RT fluorescence spectrum of Nd<sup>3+</sup>-doped MgO ceramic (black) covering the spectral range of  $^4F_{3/2} \rightarrow ^4I_{13/2}$ ,  $^4F_{3/2} \rightarrow ^4I_{11/2}$  and  $^4F_{3/2} \rightarrow ^4I_{9/2}$  inter-multiplier transitions. The fluorescence spectrum of Nd<sup>3+</sup>-doped YAG for the same range of transitions is shown (in red) for comparison. b) Fluorescence decay from the  $^4F_{3/2}$  manifold of Nd<sup>3+</sup> in MgO.

**Note:** A.u. = arbitrary units

## 4.2 Er<sup>3+</sup>:MgO

The samples of Er<sup>3+</sup>:MgO ceramic have achieved a high level of transparency, as shown in Fig. 4a, particularly in the near-infrared spectral range, as can be seen in Fig. 4b. This has enabled us to perform both absorption and emission characterization of fully densified Er<sup>3+</sup>-doped MgO ceramics. As already mentioned in the introduction, the eye-safe laser operation with resonant pumping is the most practical and critical for ultimate power scaling of lasers based on Er<sup>3+</sup>-doped materials. For this reason, our focus was on spectroscopic characterization

of  $\text{Er}^{3+}:\text{MgO}$  ceramics as it relates to resonantly pumped eye-safe laser operation originating from  $^4\text{I}_{13/2}$  level.

### 4.3 Emission

For the upper laser level lifetime measurements, which are very critical for further laser emission cross-section estimates, the excitation of  $\text{Er}^{3+}$  ions in MgO ceramic was accomplished using  $\sim 5$ -ns pulses from an optical parametric oscillator (OPO) described in Section 1.1. It was found that the fluorescence decay from the  $^4\text{I}_{13/2}$  state is single-exponential (Fig. 7). This is pretty much expected for samples with relatively low concentration of  $\text{Er}^{3+}$  when interaction between the neighboring  $\text{Er}^{3+}$  ions, as well as  $\text{Er}^{3+}$  and uncontrollable impurity ions, is negligible. The measured lifetime values for all studied samples were found to be in the range of  $\sim 14$ – $24$  ms, depending on the temperature. It should be noted that these values are considerably higher than those observed in a majority of  $\text{Er}^{3+}$ -doped oxides.<sup>18,19</sup>

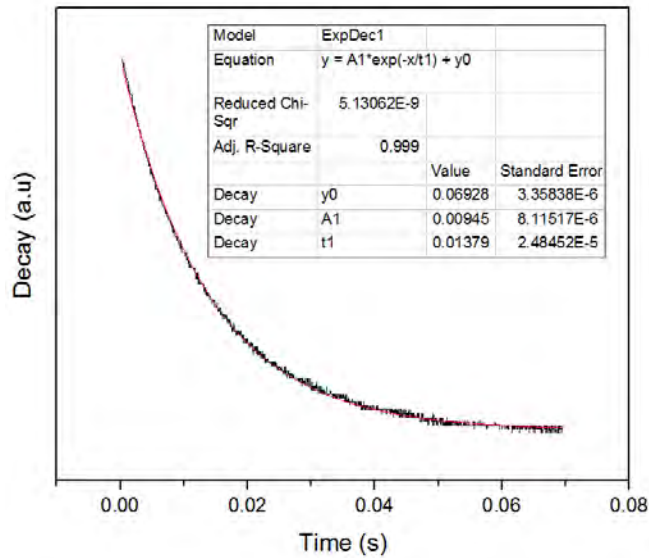


**Fig. 7**  $^4\text{I}_{13/2} \rightarrow ^4\text{I}_{15/2}$  fluorescence kinetics of fully densified  $\text{Er}^{3+}$ -doped MgO ceramic at room temperature

Figure 8 indicates the  $^4\text{I}_{13/2} \rightarrow ^4\text{I}_{15/2}$  fluorescence spectra of our  $\text{Er}^{3+}$ -doped MgO samples for a range of temperatures between 10 and 300 K. The spectra were fully corrected for spectral response of our spectrometer. While on a relative scale, Fig. 8 clearly indicates that with temperature reduction from 300 to 10 K the peak emission cross sections are increasing by about an order of magnitude. At 10 K the emission spectrum clearly exhibits the six relatively strong spectral components at 1538.1, 1540.5, 1543.0, 1563.3, 1573.6, and 1574.0 nm (indicated by arrows in Fig. 8), which is consistent with nearly single-site  $\text{Er}^{3+}$  ion occupation in MgO.

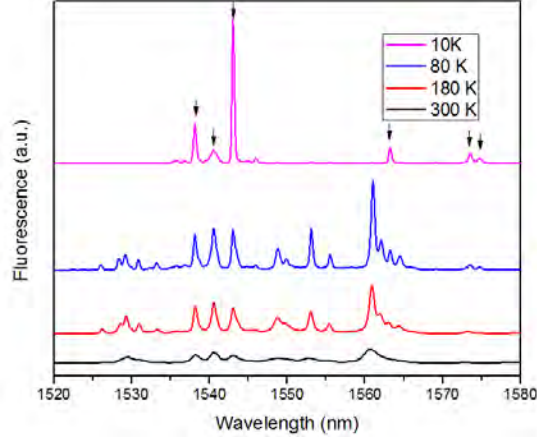


**Fig. 8** Fluorescence spectra of  $\text{Er}^{3+}$  doped MgO fully densified ceramic corresponding to the  $^4\text{I}_{13/2} \rightarrow ^4\text{I}_{15/2}$  transition in the temperature range of 10–300 K.

**Note:** A.u. = arbitrary units

From the measured fluorescence spectra and the radiative lifetime,  $\tau$ , of the  $^4\text{I}_{13/2}$  multiplet one can derive the stimulated emission cross section using the well-known Fuchtbauer-Ladenburg relation:<sup>20</sup>

$$\sigma_{emi} = \frac{\eta \lambda^5}{8\pi n^2 c \tau \int \lambda I(\lambda) d\lambda} \quad (2)$$

where  $\sigma_{emi}$  is the emission cross section,  $\eta$  is the fluorescence quantum efficiency,  $\lambda$  is the fluorescence wavelength, and  $n$  and  $c$  are the host refractive index and the light velocity, respectively. It should be noted that for our cross-section derivation the longest measured lifetimes, 14 ms, 20 and 24 ms at RT, 80 and 10 K, respectively, were used. This is based on an assumption that in the samples exhibiting the longest fluorescence lifetime the nonradiative quenching processes are negligible and, thus, the observed  $^4\text{I}_{13/2} \rightarrow ^4\text{I}_{15/2}$  transition lifetime is purely radiative (as required for the Fuchtbauer-Ladenburg treatment). For the same reason, with these longest lifetimes chosen for an estimate, the fluorescence quantum efficiency  $\eta$  of this transition is assumed to be  $\sim 1.0$ .

The emission cross-section spectrum of the  $^4\text{I}_{13/2} \rightarrow ^4\text{I}_{15/2}$  transition obtained from the above derivation is presented in Fig. 9 for the 3 temperatures, 10, 80, and 300 K. As can be seen from Fig. 9,  $\text{Er}^{3+}$  ion in MgO ceramic host has the cross-section values quite adequate for an efficient laser, in fact, very similar to those observed for the well-studied  $\text{Er}^{3+}:\text{YAG}$ .<sup>21</sup> Thus, considering very high thermal conductivity of MgO host compared to YAG, the  $\text{Er}^{3+}$ -doped MgO ceramic should be suitable for efficient laser operation based on the  $^4\text{I}_{13/2} \rightarrow ^4\text{I}_{15/2}$  transition, and with dramatically improved power scalability.

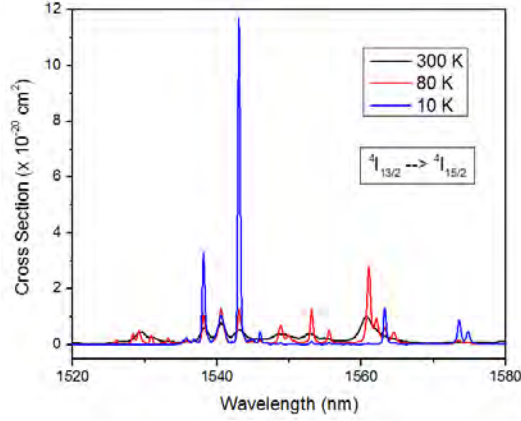


**Fig. 9** Emission cross section of the  $^4I_{13/2} \rightarrow ^4I_{15/2}$  transition at RT (300 K, black) and cryogenic temperature (80 K, red, and 10 K, blue) in  $\text{Er}^{3+}$ -doped MgO ceramic derived from Fuchtbauer-Ladenburg relation (Eq. 2)

#### 4.4 Absorption

The absorption spectra of  $\text{Er}^{3+}$  in MgO ceramic corresponding to the  $^4I_{15/2} \rightarrow ^4I_{13/2}$  inter-multiplet transitions are shown in Fig. 10 for the range of temperatures of 10–300 K. The absorption spectrum at 10 K exhibits 7 lines at 1526.0, 1528.3, 1529.1, 1530.8, 1538.0, 1540.5, and 1543.4 nm, indicated by arrows in Fig. 10. This is consistent with single-site  $\text{Er}^{3+}$  ion occupation in MgO, where the line count predicted by theory for transitions to a multiplet with the J-number of  $\{13/2\}$  is seven. Thus, this time from absorption measurements, we have a clear indication that  $\text{Er}^{3+}$  ion occupies a very well-determined single site in the MgO crystalline lattice. Based on the sample preparation technology, among other considerations, we believe that it occupies the position of  $\text{Mg}^{2+}$  ion in the MgO lattice, with the charge compensation achieved by  $\text{Li}^+$  ion co-doping.

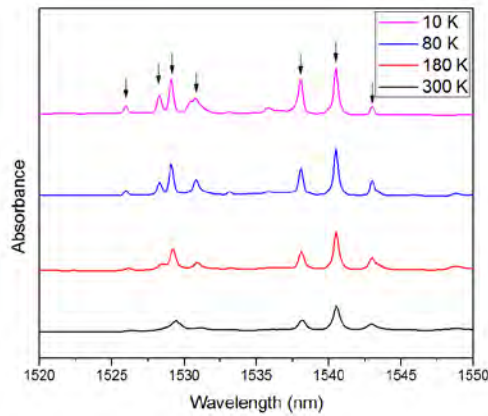


**Fig. 10** Absorption spectra of  $\text{Er}^{3+}$ -doped MgO ceramic corresponding to the  $^4I_{15/2} \rightarrow ^4I_{13/2}$  inter-multiplet transitions in the temperature range of 10–300 K. Color-coding of the plots by temperature is presented on the inset.

The energy level structure of the second excited manifold of  $\text{Er}^{3+}$  in  $\text{MgO}$ ,  $^4\text{I}_{11/2}$ , is also of significant practical importance since  $\text{Er}^{3+}$ -based solid-state lasers with eye-safe  $^4\text{I}_{13/2} \rightarrow ^4\text{I}_{15/2}$  lasing can also be efficiently pumped through this level ( $^4\text{I}_{15/2} \rightarrow ^4\text{I}_{11/2}$ ). The advantage in this case is that the most efficient and best developed commercially available InGaAs/aluminum gallium arsenide (AlGaAs) laser diodes at  $\sim 960\text{--}980\text{ nm}$  can be used. This “non-resonant” pumping, in fact, can be even more readily usable for power scaling with laser materials having much higher thermal conductivity than that of YAG. Indeed, much improved thermal conductivity in this case makes up for increased thermal load inevitable with  $^4\text{I}_{15/2} \rightarrow ^4\text{I}_{11/2}$  pumped laser operation with the theoretical quantum defect of  $\sim 40\%$  (versus  $\sim 5\%$  with resonant  $1530\text{-nm}$  pumping). The absorption spectra of  $\text{Er}^{3+}$ -doped  $\text{MgO}$  ceramic, corresponding to the transitions from the ground state multiplet  $^4\text{I}_{15/2}$  to all stark sublevels of the  $^4\text{I}_{11/2}$  multiplet are shown in Fig. 11 for the range of temperatures of  $10\text{--}300\text{ K}$ .

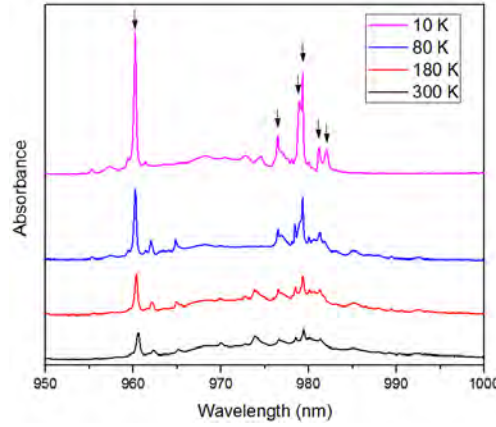


**Fig. 11** Absorption spectra of  $\text{Er}^{3+}$  doped  $\text{MgO}$  ceramic corresponding to the  $^4\text{I}_{15/2} \rightarrow ^4\text{I}_{11/2}$  inter-multiplet transitions in the temperature range of  $10\text{--}300\text{ K}$ . Color-coding of the plots by temperature is presented on the inset.

The absorption spectrum at  $10\text{ K}$  corresponds to the transitions from the lowest Stark sublevel of the ground state multiplet  $^4\text{I}_{15/2}$  (“0”-level) to all Stark sublevels of the  $^4\text{I}_{11/2}$  state. At this temperature we observed all six spectral components expected theoretically for the transitions to the multiplet with the J-number of  $\{11/2\}$ :  $960.2$ ,  $976.5$ ,  $979.0$ ,  $979.4$ ,  $981.2$ , and  $982.0\text{ nm}$ . These  $^4\text{I}_{15/2} \rightarrow ^4\text{I}_{11/2}$  transitions are indicated by arrows in Fig. 11.

## 5. Conclusions

This work presents the results of development and comprehensive characterization of fully densified  $\text{Er}^{3+}:\text{MgO}$  and  $\text{Nd}^{3+}:\text{MgO}$  transparent ceramics motivated by the ultra-high thermal conductivity of the  $\text{MgO}$  host with major emphasis on potential

laser applications. This thermal conductivity, which drastically exceeds that of conventional laser host YAG, points to potential material application in lasers with significantly improved power scaling at RT. Spectroscopic characterization provides sufficient evidence that the trivalent Er and Nd ions can be successfully doped into MgO host despite the significant ionic radius and ion charge mismatch between the dopant and the  $\text{Mg}^{2+}$  cation. The observed  $\text{Er}^{3+}$  and  $\text{Nd}^{3+}$  ion spectra in fully densified MgO ceramics exhibit clear manifestation of the dopant incorporation into purely crystalline environment. For  $\text{Er}^{3+}$  ions in MgO ceramics the single-site nature of activation was also conclusively demonstrated with the Er concentration level up to 0.156 at % usually sufficient for most efficient laser demonstrations.

To the best of our knowledge, reported here is the first successful demonstration of RE ion doping into highly thermally conductive MgO host. The presented detailed spectroscopic study of the first 3  $\text{Er}^{3+}$  ion multiplets in fully densified polycrystalline MgO material can be successfully used for future power projections and development of high power  $\text{Er}^{3+}$ :MgO-based lasers.

## 6. References

---

1. Fan TY, Ripin DJ, Aggarwal RL, Ochoa JR, Chann B, Tilleman M, Spitzberg J. IEEE J. Sel. Topics Quantum Electron. 2007;13:448.
2. Tokita S, Kawanaka J, Fujita M, Kawashima T, Izawa Y. Appl. Phys. B. 2005;80:635.
3. Zapata T, Ripin D J, Fan TY. Opt. Lett. 2010;35:1854.
4. Sanamyan T, Pavlacka R, Gilde G, Dubinskii M. Optical Materials. 2013;35:821.
5. Merkle LD, Sutorik AC, Sanamyan T, Hussey LK, Gilde G, Cooper C, Dubinskii M. Opt. Mat. Express. 2012;2:78.
6. Sato Y, Akiyama J, Taira T. Opt. Mat. Express. 2013;3:829.
7. Slack GA. Phys. Rev. 1962;126:42.
8. Charvat FR, Kingery WD. J Amer. Ceram. Soc. 1957;40:306.
9. Kuck S, Heumann E, Karner T, Maaroos A. Opt. Lett. 1999;24:966.
10. Moulton P, Mooradian A, Chen Y, Abraham M. Amer. Ceram. Soc. Bulletin. 350. 1980.
11. Ikesue A, Aung L, Taira T, Kamimura T, Yoshida K, Messing GL. Ann. Rev. Mater. Res. 2006;36:397.
12. Miles GD, Sambell RAJ, Rutherford J, Stephenson GW. Trans. Brit. Ceram. Soc. 1967;66:319.
13. Tran TB, Hayun S, Navrotsky A, Castro RHR. J. Am. Ceram. Soc. 2012;95:1185.
14. Gu F, Li C, Cao H, Shao W, Hu Y, Chen J, Chen A. J. Alloys Cmpds. 2008;453:361.
15. Apetz R, van Bruggen MPB. J. Am. Ceram. Soc. 2003;86:480.
16. Huie J C, Dudding CB, McCloy J. Proc. SPIE 2007;6545:65450E.
17. Sanamyan T, Simmons J, Dubinskii M. Laser Phys. Lett. 2010;8:569.
18. Ter-Gabrielyan N, Dubinskii M, Newburgh G, Michael A, Merkle L. Opt. Express. 2009;17:7158.



19. Payne SA, Chase LL, Smith LK, Kway WL, Krupke WF. IEEE. J. Quant. Electron. 1992;28:2619.
20. Aull F, Jenssen HP. 1982 IEEE J. Quantum Electron. 1982;QE -18:925.
21. Setzler D, Francis MP, Young YE, Konves JR, Chicklis EP. IEEE J. Sel. Top. Quantum Electron. 2005;11:645.

## List of Symbols, Abbreviations, and Acronyms

---

AlGaAs	aluminum gallium arsenide
A.U.	arbitrary unit
Cr	chromium
Er	erbium
$\text{Er}(\text{NO}_3)_3 \cdot x\text{H}_2\text{O}$	erbium(III) nitrate pentahydrate
$\text{Er}_2\text{O}_3$	erbium oxide
HIP	hot isostatic pressure
ICP-AES	inductively coupled plasma-atomic emission spectroscopy
InGaAs	indium gallium arsenide
Li	lithium
$\text{Li}_2\text{CO}_3$	lithium carbonate
$\text{LiYF}_4$	yttrium lithium fluoride
Mg	magnesium
MgO	magnesium oxide
Nd	neodymium
$\text{Nd}(\text{NO}_3)_3 \cdot 6\text{H}_2\text{O}$	neodymium(III) nitrate hexahydrate
$\text{Nd}_2\text{O}_3$	neodymium oxide
Ni	nickel
OPO	optical parametric oscillator
PEG	poly(ethylene glycol)
RE	rare earth
RT	room temperature
SEM	scanning electron microscope
Si	silicon
SSCC	solid-state crystal conversion
TC	thermal conductivity

Ti	titanium
TM	transition metal
XRD	x-ray diffraction
YAG	yttrium aluminum garnet

1 DEFENSE TECHNICAL  
(PDF) INFORMATION CTR  
DTIC OCA

1 US ARMY RESEARCH LAB  
(PDF) RDRL CIO LT TECHL PUB

1 GOVT PRNTG OFC  
(PDF) ATTN A MALHOTRA

1 US ARMY RESEARCH LAB  
(PDF) RDRL SEE L  
T SANAMYAN

2 US ARMY RESEARCH LAB  
(PDF) RDRL WMM A  
R PAVLACKA  
C COOPER

10 US ARMY RESEARCH LAB  
(PDF) RDRL SEE L  
G NEWBURGH  
J ZHANG  
L MERKLE  
M DUBINSKIY  
N TER-GABRIELIAN  
V FROMZEL  
Z FLEISCHMAN  
A OKISHEV  
R PATTNAIK  
Y CHEN